

OPTICAL AND MECHANICAL DESIGN OF THE CHARA ARRAY ADAPTIVE OPTICS

X. CHE^{*,||}, L. STURMANN[†], J. D. MONNIER^{*},
T. A. TEN BRUMMELAAR[†], J. STURMANN[†], S. T. RIDGWAY[‡],
M. J. IRELAND[§], N. H. TURNER[†] and H. A. MCALISTER[¶]

^{*}Astronomy Department, University of Michigan, Ann Arbor
MI 48109, USA

[†]The CHARA Array, Mount Wilson Observatory
Mount Wilson, CA 91023, USA

[‡]National Optical Astronomy Observatory
Tucson, AZ 85726, USA

[§]Department of Physics and Astronomy, Macquarie University
NSW 2109, Australia

[¶]Astronomy Department, Georgia State University
Atlanta, GA 30303, USA

^{||}xche@umich.edu

Received 2013 June 28; Revised 2013 October 11; Accepted 2013 October 27; Published 2014 January 6

The CHARA array is an optical/near infrared interferometer consisting of six 1-meter diameter telescopes with the longest baseline of 331 m. With high angular resolution, the CHARA array provides a unique and powerful way of studying nearby stellar systems. In 2011, the CHARA array was funded by NSF-ATI for an upgrade of adaptive optics systems to all six telescopes to improve the sensitivity by several magnitudes. The initial grant covers Phase I of the adaptive optics system, which includes an on-telescope Wavefront Sensor and fast tip/tilt correction. We are currently seeking funding for Phase II which will add fast deformable mirrors at the telescopes to close the loop. This paper will describe the design of the project, and show simulations of how much improvement the array will gain after the upgrade.

Keywords: Instrumentation: adaptive optics, interferometers; methods: numerical.

1. Introduction

The Center for High Angular Resolution Astronomy (CHARA (ten Brummelaar *et al.*, 2005, 2008)) is an optical interferometer, located at Mountain Wilson Observatory in California and operated by Georgia State University (GSU). It has six telescopes, arranged in a Y configuration with baselines from 33 to 331 m. With sub-milliarsecond angular resolution, the CHARA array can resolve nearby stellar systems, including multiple-object systems, circumstellar disks, rapid rotating stars and spotted

stars. More than 90 science papers have been published with observations at CHARA since commissioning in 2004.

To extend the target pool of fainter objects and improve the science results of bright ones, we have started to install Adaptive Optics (AO) systems on each of the telescopes to correct the atmospheric turbulence. Currently, CHARA has been funded by NSF-ATI for Phase I AO (Ridgway *et al.*, 2008; ten Brummelaar *et al.*, 2012). During this phase, we will mainly modify the current optics in telescope domes to prepare for full AO systems and install Wavefront Sensors (WFSs). The WFSs and the modified tip/tilt (TT) systems will close the loop. In the

^{||}Corresponding author.

meantime CHARA has been applying for the funds for Phase II AO, which will add a fast deformable mirror (DM) on each telescope to perform full AO correction.

The WFS systems will operate in the wavelength of 600–1000 nm. The lower wavelength bound is set to maximize the number of input photons while minimizing the atmospheric refraction effect. The upper wavelength bound is set to be below the wavelength of the infrared science beams.

One of the key science goals of the AO upgrade is for imaging Young Stellar Objects (YSOs) in the Near InfraRed (NIR) to study the evolution of the innermost disks and their interactions with the central objects. The practical sensitivity of the current system is of $R \sim 12$ and $H \sim 8$, covering 11 known YSOs in Taurus. After the Phase I upgrade, we expect about 50 of them will be observable as illustrated in Fig. 1.

In addition to YSOs, a few new classes of objects will be observable with CHARA for the first time. In particular, the brightest few Active Galactic Nuclei (NGC 4151, NGC 1068, Whirlpool) with K magnitude of ~ 9 will be within the reach of CHARA following the full upgrade. A few brightest microquasars (e.g. SS433, K magnitude 8.2) will also be observable. While the VLTI and Keck Interferometers have had this level of sensitivity for some years, they lacked the >300 m baseline that CHARA affords and the high angular resolution is needed for these objects to resolve the rather compact emission in the NIR.

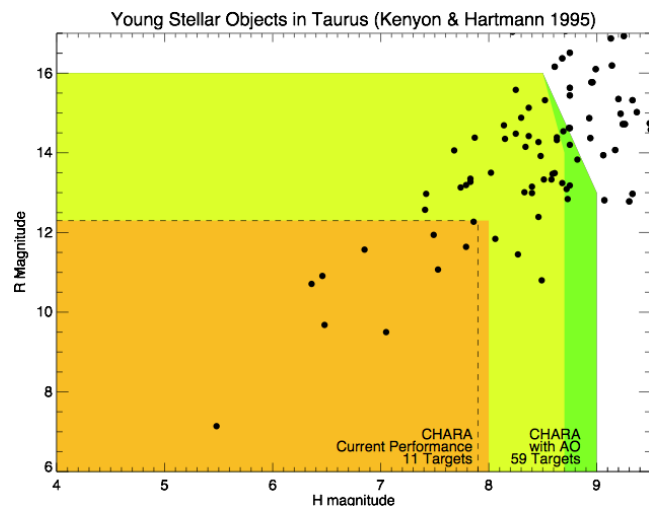


Fig. 1. YSO in Taurus. Currently ~ 11 targets are observable at CHARA, and we expect to observe ~ 59 targets after the full AO upgrade.

The AO upgrade will also improve the data quality for high-precision science. Most of CHARA targets are bright ones, which will provide enough photons for good AO correction even under poor seeing conditions. This will boost sensitivity by an order of magnitude and allow high quality observations for a higher fraction of the observing season.

We had a committee review in January 2013 to review the design of the optics and WFS. Since then we have been constructing and testing the prototype of the first Phase I AO system in the lab. We expect to install the first prototype on one of the six telescopes in August 2013, and the rest by the end of the same year.

In this paper, we first give a brief overview of the current CHARA array in Sec. 2. The CHARA AO system can be further divided into two subsystems: optical feed system and WFS which are discussed in Secs. 3 and 4. At last we will show the performance of the AO system using a simulation.

2. Overview of the Current CHARA Array

The optics of the six ALT-AZ telescopes in the CHARA array consist of a 1 m F/2.5 concave parabolic primary mirror (M1) and a confocal 0.14 m convex parabolic secondary mirror (M2). The 0.125 m collimated output beam is guided along the elevation and azimuth axes of the telescope by flat mirrors M3, M4, M5 and M6 as shown in Fig. 2. The central obscuration is 25% of the surface of the primary mirror determined by M3. The beam between M4 and M5 is easily accessible. This is where an image acquisition telescope and various alignment systems are mounted. This is also where the new AO system will be installed.

Figure 3 shows the beam path from a telescope to the lab. The light collected in the six telescopes are guided through six individual vacuum pipes into the Beam Combination Laboratory. The compensation of optical path difference is accomplished in two stages. The first occurs in vacuum and employs six parallel systems dubbed the “Pipes of Pan” (PoP). Remotely actuated mechanisms move mirrors to select appropriate DC delay segments. Upon exiting the PoPs, the beams leave vacuum and are injected into the continuous delay lines by a pair of flats. The Optical Path Length Equalizers (OPLEs) utilize cats-eye retro-reflectors on steel rail

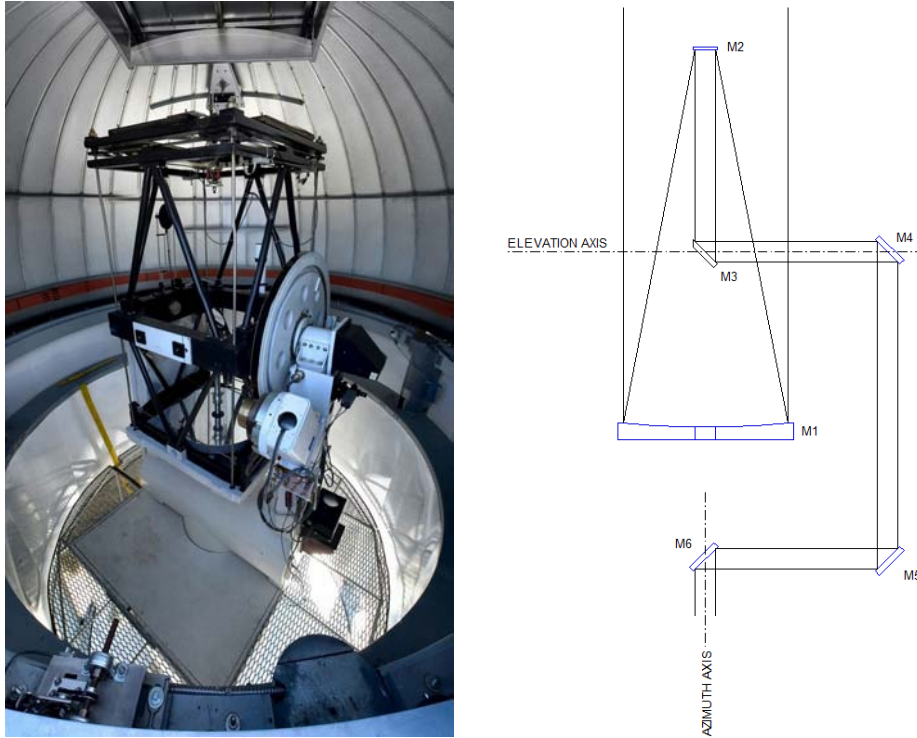


Fig. 2. One of the CHARA's six 1-m aperture telescopes. The left is a real telescope picture, and the right is a schematic drawing of telescope optics in dome.

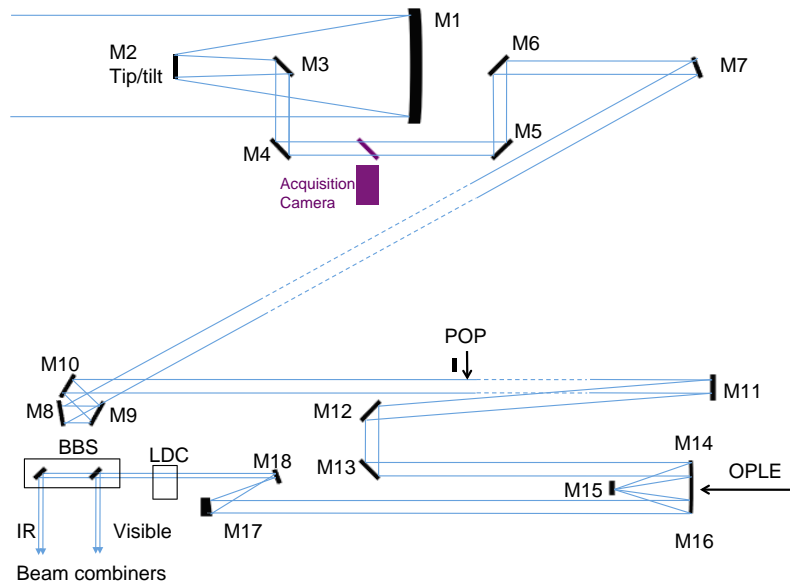


Fig. 3. Schematic drawing of CHARA beam path up to the beam combiners. The drawing is not in scale.

pair 46 m long and are controlled by a 4-tiered servo system utilizing laser metrology feedback to achieve positioning to $RMS = 10$ nm.

The beams emerging from the OPLEs are reduced to a final diameter of 1.9 cm by beam-reducing telescopes. The beams then pass through

longitudinal dispersion correctors (LDC) that correct for unequal air paths. Finally, the Beam Sampling System (BSS) separates visible from IR light at the $1\text{-}\mu\text{m}$ boundary and turns the two beams through 90° along parallel paths to the visible and IR beam combiners. Each BSS assembly

also selects baseline pairs to be directed to the beam combiners.

Through formal collaborations with several institutions, the beam combination laboratory contains seven separate combiners with complementary regimes of wavelength, sensitivity, and measurement precision. These include:

- CHARA Classic: a two-beam J, H, K open-air beamsplitter-based system providing moderate-accuracy visibilities (5%) at moderate sensitivity limits ($K = +8.5$) developed by CHARA staff (Sturmann *et al.*, 2001).
- FLUOR: a two-beam single-mode fiber-based K-band beam combiner achieving our highest accuracy in V^2 (0.2%) at the expense of sensitivity ($K = +5.0$). It is a collaboration with the Paris group (Lhome *et al.*, 2012).
- MIRC: a single-mode based all-in-one six-telescope beam combiner, operating in H (sensitivity ~ 6) and K band. It was developed at University of Michigan (Che *et al.*, 2012).
- VEGA: a four-beam high spectral resolution ($R = 30,000$) visible light instrument developed at l'Observatoire de la Côte d'Azur (Mourard *et al.*, 2012).
- PAVO: a three-beam, low spectral resolution visible light combiner developed at University of Sydney. The same beam combiner is also developed at Sydney University Stellar Interferometer (SUSI) (Ireland *et al.*, 2008).
- CHAMP: a six-beam, pair-wise open-air beam combiner to provide phase tracking and group delay information for other beam combiners. It was developed at University of Michigan (Monnier *et al.*, 2012).
- CLIMB: two three-way beam combiners to obtain J, H, and K closure phases using two three-telescope sets. It was developed by CHARA staff (see ten Brummelaar *et al.* in the same issue).

The Array control system is based largely on Linux except for the OPLE subsystem, which runs under $V \times$ Works. During 2011, a new Linux-based telescope control system has been put online to replace the aging DOS-based system. While Array Operations are usually conducted from Mount Wilson, remote operation facilities exist in Atlanta, Paris, Nice, Sydney, Ann Arbor and Bonn. We expect that the new AO system will also be built on an RT-Linux based control system.

3. Optical Feed System

3.1. Telescope

Currently, the array operates with an actuated tip/tilt mirror (M2) controlled by a TT detector in the laboratory. Putting the TT detector in the laboratory is advantageous because it can detect angular beam errors in the whole optical train. Also a single CCD camera can serve all six telescopes. On the other hand this arrangement suffers from low sensitivity due to losses on the numerous mirrors along the path. Due to these losses, only objects $R < 12$ can be tracked.

In Phase I of the AO project, a WFS will be installed on each telescope and will be used initially to drive the TT mirror. Placing the TT detector at the telescopes will increase sensitivity but necessitates a separate slow tip/tilt system in the laboratory to measure turbulence between the telescopes and the laboratory. In Phase II of the project a deformable mirror will replace M4 and the system will work as a low order AO system.

3.2. Optical layout

The first optical element in the new AO system is a beam-splitter, 6.25 in in diameter, between M4 and M5. Figure 4 shows the optical layout of CHARA AO system. The angle of incidence is 10° . Since there are numerous beam combiners operating in different wavelength regimes available at CHARA, there will be a need to split the light differently between TT detection and interferometry depending upon the beam combiner used. There will be three beam-splitters available.

The new WFS is a EMCCD, thus one of the beam-splitters will be a dichroic mirror which reflects most photons below $1\mu\text{m}$ toward the tip/tilt detector. The IR photons will pass through the beam-splitter for interferometry. The beam reflected by the dichroic mirror will be focused by a commercial 6-inch F/4 parabolic mirror (m1) (Edmund Optics #32-069-533). Before the focus, a small elliptical flat mirror (m2, overall view in Fig. 4 and zoom-in view in Fig. 5) (Edmund Optics #32-132) will intercept the beam to place the focus in a more convenient place. The mirror is small enough to be hidden in the shadow cast by M3. The focus of the parabolic mirror will pass through a $120\mu\text{m}$ laser drilled hole in small flat mirror (m3, shown in Fig. 5) (Edmund Optics #84-410). Light from the science object will pass through the

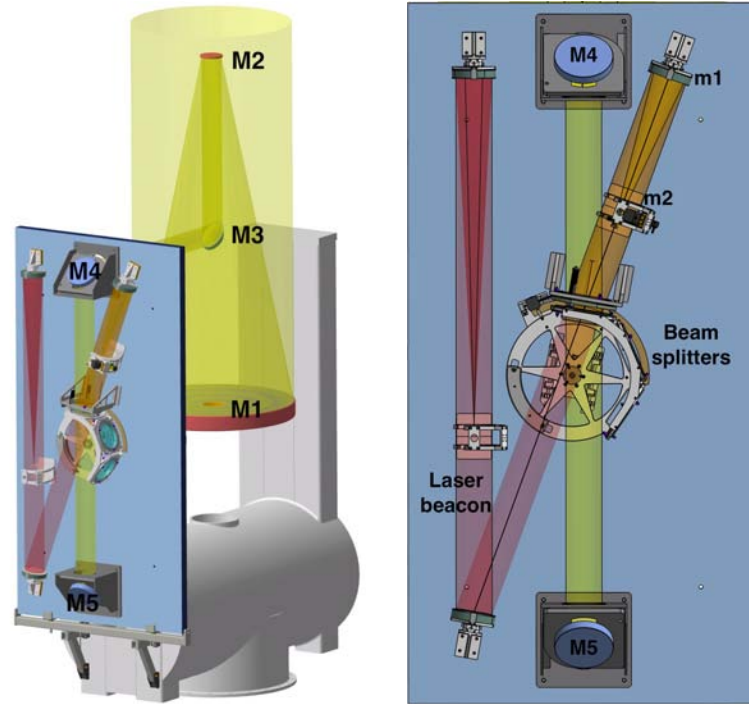


Fig. 4. The schematic drawing of AO optics. Left is a 3D view of the telescope optics with AO system. Right is a face-on view of the AO system. The light propagates in the order of M1, M2, M3, M4, and then gets split. The reflected light goes through m1, m2, m3, and then enters into the acquisition camera and WFS. The rest light propagates to M5 and other optics into the Beam Combination Laboratory.

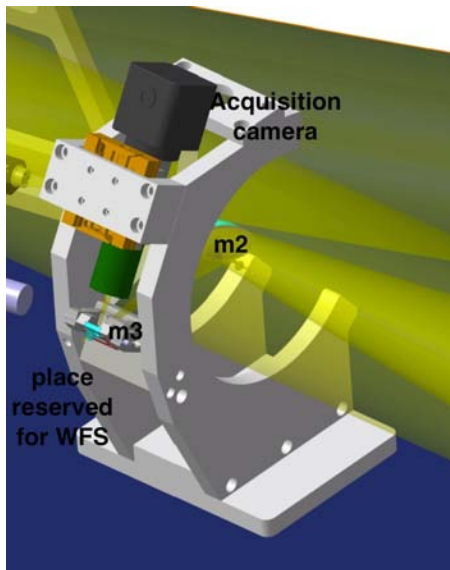


Fig. 5. One end of the laser fiducial system. The m3 mirror has a hole in the center. The light bounced off m2 is partially reflected by m3 upwards into acquisition camera, and the rest goes through the hole of m3 and enters WFS.

hole undisturbed toward the WFS, while the rest of the field will be reflected toward a 1:1 relay optic (Edmund Optics #45-759) followed by an 1/2" analog image acquisition camera (Astrovid

Stellacam II). The nominal effective focal length is 4876 mm. The projected size of the pinhole is 5 arcsecs on the sky. The acquisition field is 3.4×4.5 arcmins at a pixel scale of 0.42 arcsecs/px.

The light passing through the hole of m3 enters the WFS system, which will be discussed in Sec. 4.

3.3. Laser fiducial

There are certain features in the old system which are essential to keep in the new system. One of them is the use of a laser fiducial for co-aligning the telescope pointing axis and the rest of the optical system. The optical paths between the telescopes and beam-combiners are several hundred meters long and therefore the field of view in the laboratory is extremely narrow (<10 arcsecs). Finding a star would be a daunting task without using a laser for aligning the telescopes. A full size laser beam, nominally 0.125 m in diameter, can be sent out to each telescope from the laboratory. The same laser is used to align the beam-combiners in the laboratory. The laser beam is centered at the telescopes between M4 and M5 by adjusting a mirror (M10) in the laboratory. A 1-inch corner-cube in front of

M2 intercepts the laser beam and reflects it back toward the acquisition telescope. The acquisition camera (shown in Fig. 5) picks up light from both the laser and from the target star so the observer sees a stationary “laser star” and the target star in the field. The telescope is moved until the two images are coincident. When this happens, the TT detector takes control of centering the beam in the laboratory for beam combination. The difference between the new and old systems in this respect is that in the old system the corner-cube is centered in the beam and permanently mounted in front of M2, while it has to be off-center in the new system otherwise the small flat mirror (m3) in front of the parabolic collimator mirror (m2) would block the laser beam from reaching the acquisition camera. When the object is acquired the corner-cube will be moved out of the beam. The moving mechanism can be simple, since the corner-cube is not sensitive to tilt. Also, in the old system the laser fiducial was allowed to drift over time due to coudé misalignment, for example, but in the new system, the laser fiducial as well as the star have to fall in the pinhole. This will require occasional tilt adjustments on the beam-splitter.

3.4. Laser beacon

Since the WFS will be at the telescope, a large non-common path from the telescope to the laboratory will not be seen by the WFS and thus cannot be corrected by the fast DM. Therefore, a separate slow WFS and small deformable mirror will be installed in each of the six telescope beams in the laboratory to measure and remove static aberrations and non-common path errors. For bright sources the science target itself will be able provide enough light for the slow WFS but for fainter objects one most likely will need a beacon at the telescope. The optical layout of laser beacon is also shown in Fig. 4. A point source (fiber tip) will be placed in the focus of a 6-inch F/8 parabolic mirror. The collimated beam will be divided by the beam-splitter. The reflected part will provide a bright point for the slow WFS in the laboratory. The transmitted beam will serve as a reference source for calibrating the WFS.

3.5. Calibration source for the DM

In Phase II, a large (126 mm × 178 mm) elliptical DM with 30–60 actuators will replace M4. A calibration source will be needed to generate the

interaction matrix, verify DM-to-WFS registration and calibrate non-common path errors in the AO optics. The calibration source will provide a full size beam and will be placed upstream from M4. One could use a spatially filtered laser in the focus of either a lens or a parabolic mirror. A lens would be simpler mechanically, because it could be mounted on the breadboard just before the DM. In that case and with a monochromatic on-axis source, only spherical aberration would need to be corrected. That could be done either by using an aspheric lens or a lens with spherical surfaces and a commercially available spherical aberration compensator plate as shown in Fig. 6.

In case of reflective optics, the parabolic mirror would be mounted on the inner wall of the mid frame of the telescope. The source could be polychromatic and would be on the breadboard in front of the DM.

3.6. Mechanical setup

For stability, the AO system will be installed on a custom breadboard (Newport IG-series 4' × 8'). The breadboard will be mounted on the side of the fork by adjustable mounting fixtures. The mounting fixtures will allow us to make the breadboard vertical, perpendicular and centered on the altitude axis. The position of the breadboard along the altitude axis is not critical. The breadboard will have two

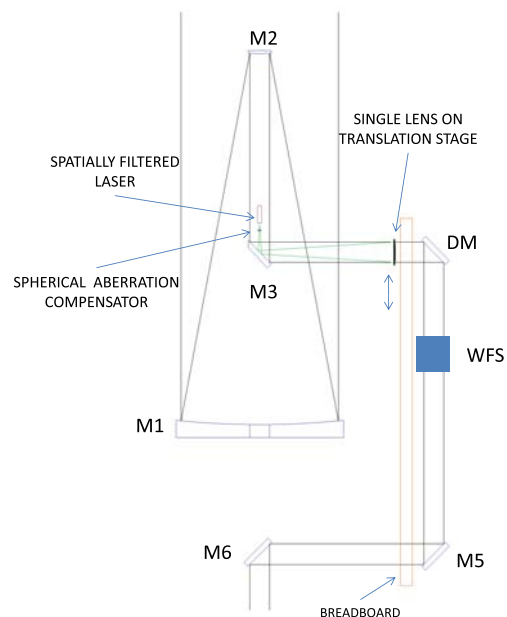


Fig. 6. The design of calibrator source for DM.

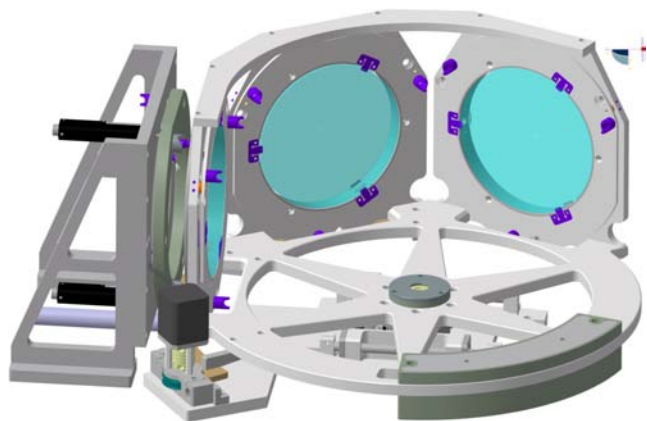


Fig. 7. Carousel system. One of the three different beam-splitters can be chosen by rotating the device.

7.5-inch holes bored for the beams to pass through between M3, M4 and M5, M6.

Three different beam-splitters will be mounted on a remotely controlled dichroic changer (carousel, Fig. 7). The carousel is designed in such a way that the beam-splitters can be rotated in their position very precisely with simple devices.

Underneath the carousel, there is a mechanism to move the whole carousel linearly toward and away from a reference ring which has three wedge-shaped hard points. The reference ring itself can be remotely actuated for tilt alignment. Each of the three beam-splitters is held in the carousel by spring-loaded cells which have three steel balls for mating with the wedges on the reference ring. During a beam-splitter change, the carousel is moved away from the reference ring by a linear actuator. When there is enough clearance, another beam-splitter is rotated into position. An error of a few degrees is tolerable. Then as the linear actuator moves the carousel back, it presses the spring-loaded beam-splitter cell against the reference ring thereby forcing the beam-splitter to the correct position and direction. To assure the proper mating of the beam-splitter cell and the wedges on the reference ring, the lateral position of the beam-splitter cell in the carousel is defined by three cones. When the beam-splitter cell gets in contact with the wedges on the reference ring and the linear actuator keeps pushing the carousel closer to the reference ring, the cones are lifted from their socket and the orientation of the splitter mount is solely determined by the reference ring. When the carousel is moving away from the reference ring, the cones are resealed and the beam-splitter cell goes back to its parking position in the carousel.

This arrangement makes it unnecessary to encode the carousel position precisely. The precision of a simple open loop stepper motor is more than adequate yet the tilts of the beam-splitters are precise. The reference ring itself can be properly tilted for each beam-splitter by encoded motors, if needed.

The 6-inch parabolic collimator (m1) and the collimator for the laser beacon will be mounted on custom fixtures which allow two precise axis tilts, and a motorized focusing translation.

4. The WFS System and the DM

The beam from Optical Feed system goes through the pinhole of the m3 mirror and enters into the WFS system (left panel of Fig. 8). A Shack-Hartmann style WFS is used because it is simple, stable, compact, and does not involve moving parts.

The WFS system contains a collimator, a lenslet array, a pair of lenses as a re-imaging system, and a camera. The collimator will be held on a linear XYZ stage (Newport, 460A-XYZ-LH), and the other parts will be mounted on another linear XYZ stage (Newport, 562-XYZ), as shown in the right panel of Fig. 8. The reason for two separate stages is to correct angular and linear deviations of the incoming beam. Figure 9 shows how the beam propagates in the WFS.

A fast DM, although not purchased during Phase I AO, is also taken into account for a complete design.

4.1. DM and lenslet array

The choices of DM are limited because of the specific requirement to replace M4 in the telescope to maximize sensitivity. The DM has to be large and elliptical, and its 45° projection has to be a circle. And the minimum number of actuators is determined by the seeing condition. Suppose the worst observable seeing condition is $r_0 = 5$ cm at 0.5 micron at CHARA, which is equivalent to 21 cm r_0 in H band. To match the r_0 in H band, the minimum numbers of actuators and lenslets across a 1-meter primary pupil are both 5. Two possible different bimorph DMs from Cilas fit these requirements: a 31-actuator (19 inner ones, 5 across the pupil) and a 61-actuator (37 inner ones, 7 across the pupil) device. These two DMs are both pseudo-hexagonal, as shown in Fig. 10. The geometries of the DMs are used in the simulation.

In order to match geometry of the DMs, an off-the-shelf hexagonal lenslet array from OKO was

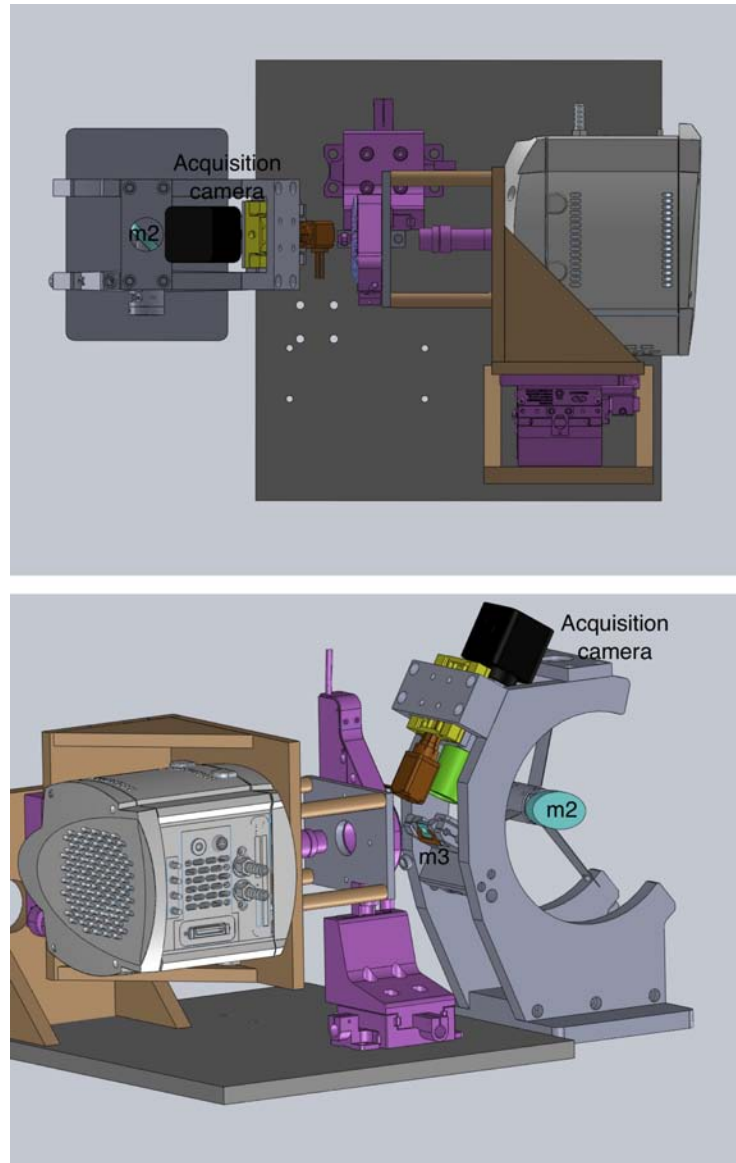


Fig. 8. Top and side view of how WFS is coupled with one end of the CHARA AO optics (Fig. 5). All WFS components are on a separate board.

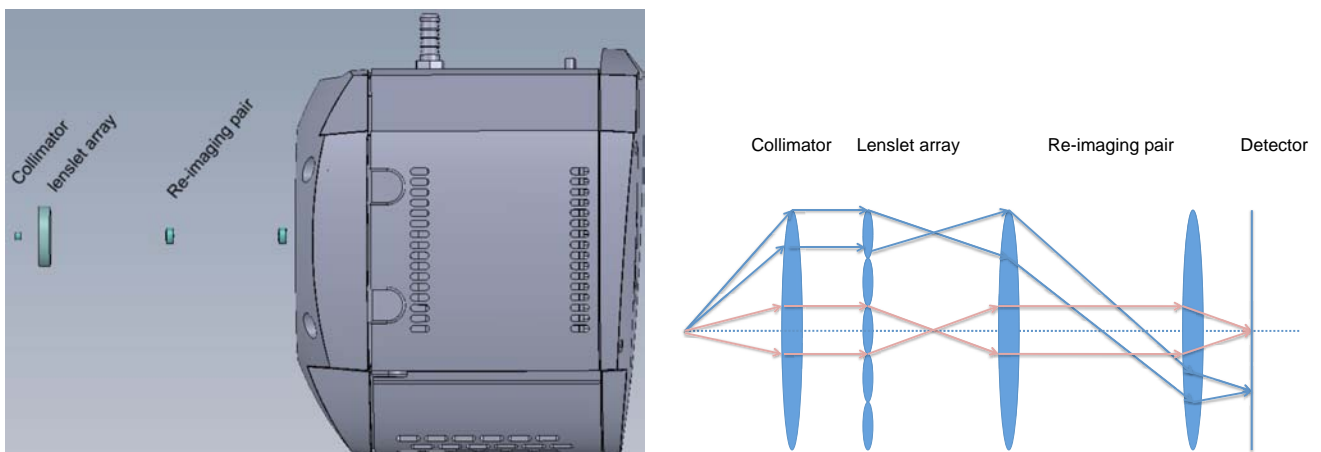


Fig. 9. Left shows the optics and the camera in WFS. Right (not to scale) shows a schematic drawing how light propagates.

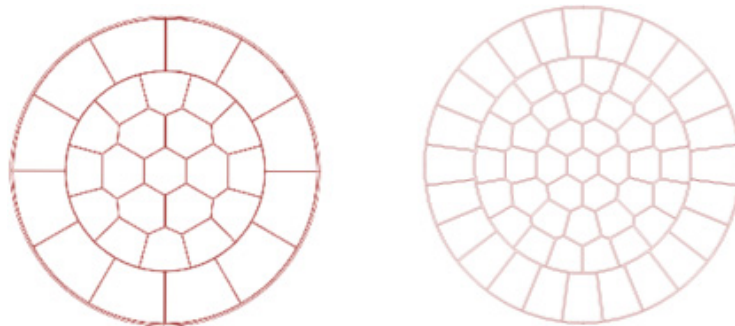


Fig. 10. Two different actuator geometries of candidate DMs from Cilas. Left has 31 actuators and right 61 actuators. These are the projected geometries of the elliptical DMs.

chosen. The lenslet array has 300-micron pitch, a focal length of 18 mm, and a 100% fill factor. One side of the lenslet array will be coated with an AR coating. The lenslet array will be placed at a plane conjugated with the M2 (tip/tilt) mirror so that moving M2 will not shift the pupil on the lenslet array. The DM however is not conjugated to M2. But the beam is slow enough that the pupil on DM is relatively stable. To be quantitative, the pupil on the DM will move in the order of 0.1 mm for every arcsecond of tip/tilt motion. This is much less than the distance between the actuators.

We have considered two lenslet configurations: 18 subapertures (5 across the pupil) and 36 subapertures (7 across the pupil). Each subaperture measures two pieces of wavefront information: x and y slopes. So on average a lenslet configuration with n subapertures is able to control a DM with $2n$ actuators. The 18-lenslet configuration roughly matches the 31-actuator DM, and 36-lenslet with 61-actuators. Although the 36-lenslet configuration

better samples wavefronts, the 18-lenslet configuration has higher sensitivity. We will compare the performance of these two configurations in the simulation in Sec. 5. The geometry and some characteristics of these two lenslet configurations are listed in Table 1 and shown in Fig. 11.

Another factor to optimize the size of the re-imaged pupil concerns the partially illuminated lenslets along the edge of the pupil. These lenslets will distort the stellar images under the diffraction limit and compromise the contained wavefront

Table 1. The two optimized projection of the pupil onto the hexagonal lenslet array.

	18-lenslet	36-lenslet
Number of illuminated lenslets	18	36
Projected pupil size (mm)	1.376	1.869
Total usable surface area ratio	93.6%	97.8%
Minimum illuminated lenslet	81%	61%

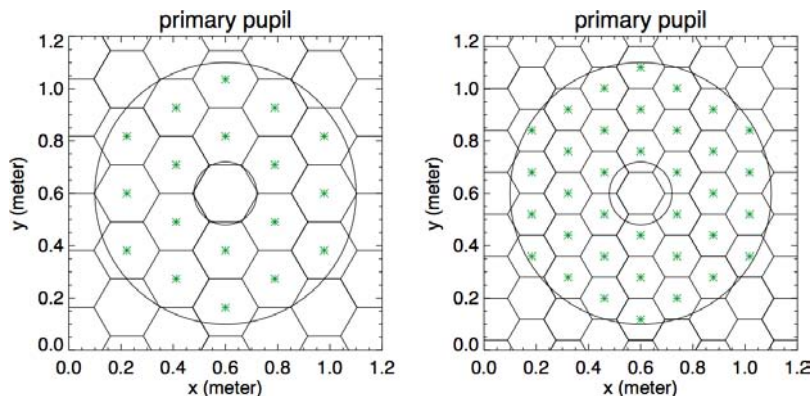


Fig. 11. The lenslet array from OKO contains 127 microlenses in a hexagonal configuration with 300-micron pitch. The two different scalings of the pupil onto the same lenslet array are shown above, corresponding to pupil size of 1.38 mm (left) and 1.87 mm (right). The large circle is the edge of the primary mirror, and the small circle is the projection of the secondary. The hexagons with stars inside are the ones that will be used to measure the wavefront.

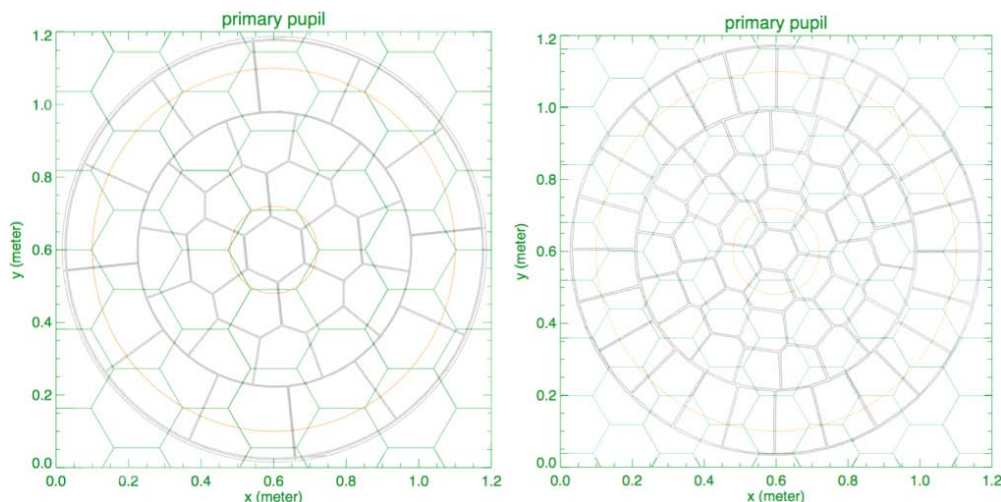


Fig. 12. (Color online) The DM devices (grey) are plotted over the two lenslet configurations (green). Left: 31-actuator device over 18-lenslet array. Right: 61-actuator over 36-lenslet array. The pupil of the telescope (orange) is also overplotted.

information. Therefore we only use the lenslets that are illuminated with most of their surface areas, and discard the ones illuminated with a small fraction. The size of the pupil on the lenslet array is optimized in a way to maximize the surface areas of useful lenslets and minimize those of discarded lenslets. Table 1 summarizes the results of the optimization.

The orientation of the lenslet array must be optimized with respect to the DM actuator positions. We maximize the distances between the centers of the DMs and the centers of lenslet arrays. The lenslet array is held by a rotation stage that can be remotely controlled (Thorlabs, PRM1Z8E). Examples of the optimal orientation are shown in Fig. 12 where the 18-lenslet array is overlapped with the Cilas 31 DM and the 36-lenslet array is overlapped with Cilas 61 DM.

4.2. Collimator

To project a re-imaged pupil with 1.87 mm diameter onto the lenslet array, an off-the-shelf $f = 9$ mm achromatic doublet (Edmund Optics # 45090) is used. We carried out a ZEMAX calculation including all optics up to the collimator: M1, M2, M3, M4, dichroic, the parabolic focusing mirror and the collimator, and found the peak-to-valley wavefront errors $\sim 1/10$ wave for two example wavelengths 600 nm and 900 nm as shown in Fig. 13. This demonstrates this off-the-shelf doublet is good enough for our purpose. For the 1.38 mm re-imaged pupil, a customized doublet will be needed.

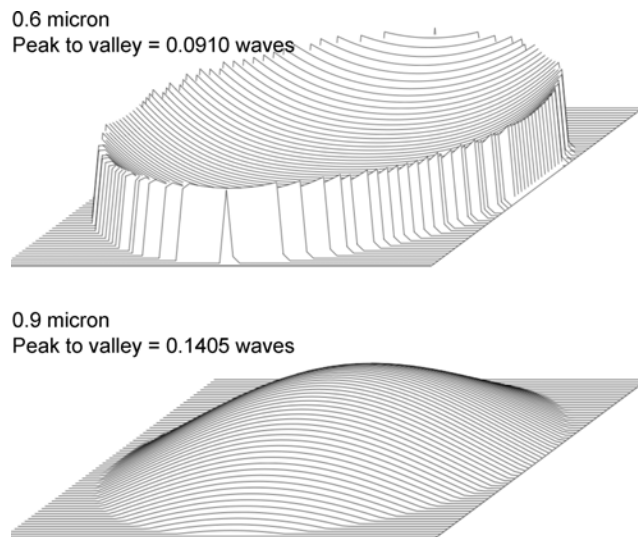


Fig. 13. The wavefront errors from a telescope to the off-the-shelf collimator based on ZEMAX calculation.

4.3. Re-imager

While the OKO lenslets has some excellent properties, the physical size is not optimal for imaging the spots onto the camera. The Shack-Hartmann spot size on the camera would be 2.7 pixel/FWHM without a re-imaging pair of lenses. Our simulation shows that a 1.5 pixel/FWHM spot is sufficient to recover wavefront information, and suffers less detector noise. To keep the telecentric spots, a pair of re-imaging lenses is used to scale down the spot size. Two off-the-shelf achromatic doublets (Edmund Optics, #49306, #49309) are chosen with focal length of 35 mm and 20 mm. Both have visible

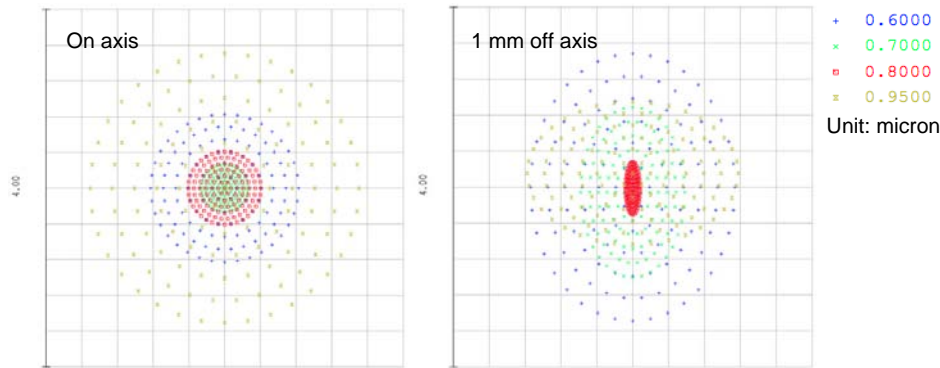


Fig. 14. The diffraction-limited images produced by the re-imaging optics for wavelength from 600 to 950 nm. Both on-axis and the furthest off-axis spot images are shown.

anti-reflection coatings to increase the throughput. In this design, the entire pupil is sampled by 67×67 pixels and each subaperture has a field-of-view of $6.7''$, sufficient for control of bad seeing ($r_0 \sim 5$ cm) even for a feed-forward system.

Figure 14 shows the result of ray tracing the re-imaging optics. We calculated the image quality using ZEMAX ray-tracing and found the spot size is well within the ~ 24 micron diffraction limit, even for the most extreme off-axis lenslet spots.

4.4. Camera

The choice of camera for this project is critical since the low-light noise performance will set the limiting magnitude for the AO system. Classical CCDs or the newer CMOS cameras are dominated by read noise with a nominal value of $3\text{--}4 e^-/\text{pixel}$ at the high frame rates needed for adaptive optics. An EMCCD is a better choice because it can amplify the signals through an avalanche-gain register readout, essentially operating with no read noise. The EMCCD suffers some drawbacks, such as root 2 higher Poisson noise when using high gain and Clock Induced Charge (CIC) noise that is indistinguishable from signals. In general, an EMCCD does not have an advantage over a classic CCD at high Signal to Noise Ratio (SNR), but is much more sensitive at low SNR due to negligible read noise. It is worth noting that most EMCCDs do not have an adequate frame rate for adaptive optics on large telescopes but it is sufficient for CHARAs 1-m aperture.

Specifically, we have decided on the Andor Ultra iXon 897. This new iXon model has $<0.005 e^-/\text{pixel}$ clock induced charge and is capable of 1 kHz frame rates for readout areas smaller than 90×90 pixels, which is sufficient for CHARA AO.

Initial tests of actual hardware confirmed these specifications using just thermoelectric coolers. We chose the commercial standard high-speed Cameralink interface and carefully selected a low latency, Linux compatible PCI card (from EPIX). Since the main science targets after this upgrade are T-Tauri stars, which have red spectra, a camera with high Quantum Efficiency (QE) at longer wavelengths is preferred. One type of CCD with deep depletion technique fits this criteria well, unfortunately the CCD substrate was not available for EMCCDs such as those used by Andor.

4.5. WFS control software

The control computer for the CHARA AO system will be a PC running CentOS 6.3. This installation is compatible across many subsystems at CHARA and leverages experience in device drivers and software infrastructure. The computer will host a PCI-based Cameralink card by EPIX that has low latency to access the Andor camera data even at highest frame rates.

The AO computer installation has the pre-emptive kernel patch that allows the system to provide real-time support for time-critical functions, such camera readout, centroid analysis, and signal output to DM electronics. This pre-emptive kernel patch has been tested to have $<10 \mu\text{s}$ latency and is in use for several other CHARA subsystems.

4.6. Data flow

We expect the software will follow a modular design, whereby multiple threads interact through shared memory to process the camera data at full frame rate with minimum latency. Here is an example data

flow:

- A Cameralink thread will detect new data from PCI bus. This thread will receive raw data from the camera and prepare it to be science ready, including bias subtraction, flat fielding, and software co-adding.
- A WFS thread will calculate the centroids from each new science frame. Next, the wavefront will be estimated using Zernike modal analysis. The tip/tilt correction will be sent to the tip/tilt mirror with appropriate gain. The rest higher order corrections will be sent to a fast DM during Phase II AO.
- The telemetry spooler will be a low priority thread that can utilize time stamps, using the standard CHARA time base, to record wavefront telemetry for future data analysis and correlation with fringe data.

The WFS will be modeled on our existing real time systems and follow a socket based client/server model. Both a prototype server and client have been developed and are now under test.

5. Simulation

The simulation package is specifically designed for the CHARA AO project. It was developed independently using IDL language. A few assumptions are made in the simulation.

- The background of the sky is about 18.5 (mag/arcsec²), and is ignored because even our faintest targets are still much brighter.
- No spectral dispersion is included. All photons are assumed to have wavelength of 0.7 micron, which is a compromise of the QE of the detector and relatively red spectra of our main science targets.
- 4.2e9 photon/s received on the detector of the WFS for an $R = 0$ magnitude target. This takes into account the transmission loss from the primary mirror to the WFS detector.

5.1. Wavefront simulation

The wavefront variation is caused by the atmospheric turbulence. We assume that the turbulence only affects the phases but not the intensities across the pupil and ignore scintillation. In reality, the turbulence could come from multiple layers. But in the simulation, we assume it comes

from only two layers with different wind speeds. The turbulence in the simulation follows the Kolmogorov model where the power spectrum of the turbulence follows a power law with the exponent $-11/3$. A cutoff of the power spectrum is set at the outer scale of 30 m. In the simulation, two different 30×30 m big phase screens are created in advance for $r_{0,\text{ref}} = 5$ cm seeing conditions at $\lambda = 0.5$ micron, then each is scaled by $(\frac{r_0}{r_{0,\text{ref}}})^{5/6}$ to simulate a phase screen at r_0 seeing conditions. r_0 at the two layers could be different. Two little pieces of phase screens are extracted sequentially and respectively out of the two big ones, and added together as the inputs to the WFS to simulate winds blow over the aperture. An example phase screen is shown in Fig. 15.

5.2. Detector simulation

The parameters of the WFS detector in the simulation use those of Andor iXon Ultra 897, including all detector noises and quantum efficiency.

The dark current rate is $0.001 e^-/\text{pix}/\text{sec}$. As the typical integration time will be 1 to 100 ms the occurrence of the dark current is negligible in the simulation.

The read noise depends on the read out rate. Assuming a 67×67 pixel array per frame and 1000 frame/s speed, the equivalent read out rate is

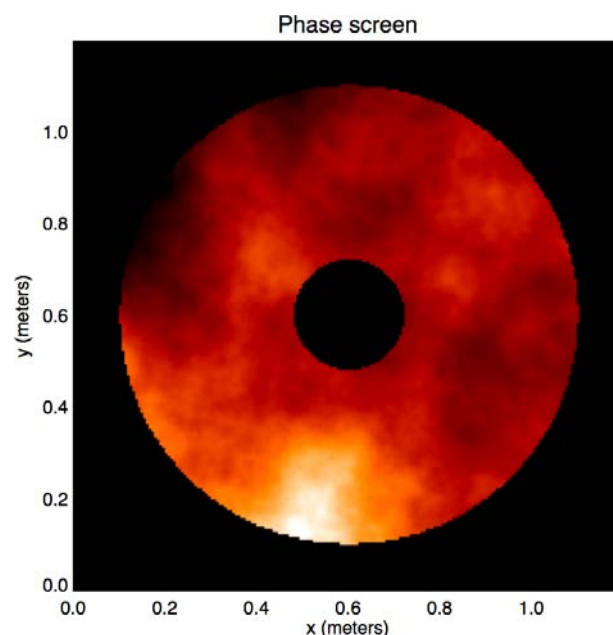


Fig. 15. A snapshot of the modeled phase screen of the atmosphere above a single telescope.

about 4.5 MHz, which corresponds to $25 e^-$ read out noise for this camera. Therefore a Gaussian distribution with a standard deviation of $25 e^-$ is used to simulate the read noise.

A high Electron Multiplier (EM) gain of the camera will amplify the real signals, but will also shorten the lifetime of a detector. Also a high EM gain will saturate the detector if the target is bright. So a high EM gain (1000) is only used for low light level, and decreases accordingly if the target gets brighter. The EM gain variation is simulated using an exponential distribution.

Since the real signals will be mostly above the read noise background after the EM gain amplification, we can use a threshold to filter out the noise. A high threshold is preferred in terms of rejecting read noise. On the other hand, as the gain has certain variation, some real photon signals will be filtered out because they are below the threshold even amplified by the EM gain. Furthermore the higher the threshold, the higher the probability that the real photon signals will be filtered out. So there is an optimal threshold that eliminates most of read noise and keeps most of real signals. In the simulation, we use threshold of $4 \times$ the RMS of read noise (typically $100 e^-$ for read noise RMS = $25 e^-$), which only has 3×10^{-5} probability of a false signal and causes approximately 10% of the real photons to be rejected.

Another important detector noise is the Clocked Induced Charge (CIC). It mostly happens when moving the charges into the EM gain registers, which is just before the gain amplification. So the CIC noise is also amplified by the EM gain, and there is no way to tell a photon signal from CIC noise. The frequency of occurrence of CIC noise is 0.005/pixel for this camera. We simulate CIC noise using a Bernoulli process. This is the dominant noise at the lowest light levels. A simple study shows that even when the signal is 4 times the CIC noise on average, there is still 27% chance that the number of electrons from CIC is equal to or greater than that from photons in a frame.

The Quantum Efficiency (QE) of the camera is the most red sensitive on the market for EMCCDs at the time of purchase. The QE is above 90% from 400–700 nm, and drops to 40% at 900 nm. The QE is only used to calculate the number of photons received. After that we assume all photons have a single wavelength 0.7 micron as mentioned above.

5.3. Centroid estimation

A 2-dimensional Gaussian fit may work better to find the centroid if there are enough photons. But for faint YSOs, we will be starved for photons most of time. Therefore a center of light algorithm is used to estimate the centroids for each subaperture:

$$\text{Centroid} = \frac{\sum n_i p_i}{\sum n_i > m} \quad (1)$$

where n_i is the number of photons for pixel i and p_i is the position. We clamp the denominator to be m to reduce the estimated centroid offset if the total number of the photons is less than m . The clamped denominator can reduce the noise of centroid estimation when there are too few photons. In our simulation, we find $m = 6$ is an optimal value. As for Phase I AO upgrade, only a fast tip/tilt correction will be implemented, we further weight the centroids of subapertures with their total photon numbers. Lastly, Hanning windows with size of 5×5 pixels ($3.1'' \times 3.1''$) are used to filter out the noise that is far from the center of each subaperture.

5.4. Wavefront reconstruction algorithms

The mean slopes of the wavefront over each subaperture can be estimated from the differences between the computed centroids and reference centroids from a flat wavefront. Then the wavefront of the whole aperture can be reconstructed from the slopes. We explored two methods to reconstruct the wavefront: zonal or modal, and found modal method is consistently better than zonal method in our case. So we will only introduce the modal method.

In the modal method, we use the Zernike modes. The number of modes that are used to recover the wavefront depends on the number of subapertures. With too few modes, the reconstructed wavefront misses some high order information measured at the WFS; while with too many modes, the high order modes basically track the noise. We find the number of Zernike modes should be comparable to the number of the lenslets, and use 21 modes for 18-lenslet configuration and 36 modes for 36-lenslet configuration.

The reconstruction is done by solving a series of linear equations forming the matrix

$$A\alpha = \beta \quad (2)$$

where α is coefficients of modes and β is the mean slope estimated from each subaperture, A is the matrix that convert wavefronts of Zernike modes into slopes. Each row of matrix A can be computed by using one corresponding Zernike mode as an input and calculating the mean slopes of each subaperture. To solve for α , matrix A needs to be inverted and this is not possible when A is not a square matrix. We therefore use Single Value Decomposition (SVD) to compute the pseudo-inversion of the matrix A . Finally the wavefront can be reconstructed by adding up all the Zernike modes with calculated coefficients.

5.5. Applying to deformable mirror

The reconstructed wavefront contains two parts: the tip/tilt component and the higher order Zernike components. The tip/tilt correction will be passed to the secondary mirror of a CHARA telescope (Phase I AO), and the rest to a fast DM for a full AO correction (Phase II AO). In the simulation, we will show the performance of both. A simple tent-like DM model is used where the centers of segments of the DM can move up and down freely and the other parts of the segments just follow these centers in a linear manner. This DM model is very preliminary mainly because we do not have the proper influence function from the manufacture. Plus the DM will not be purchased until the funding for the second phase AO is allocated. At that time we may have more options on suitable DMs that are available on the market. Therefore in the simulation, we will use this linear interpolation model for the DM. We

extract the phases of the reconstructed wavefront at the position of the centers of the DM, and then the full DM surface can be computed by linear interpolation for the rest part of the DM. A 2 ms lag is applied for the time between frame acquisition and DM correction.

The function used to calculate the DM correction is:

$$u_i = a_0 u_{i-1} + k d_i \quad (3)$$

where u_i is the actuator vector at time i , a_0 is the leaky integrator factor set to be 0.95, k is the loop gain, and d_i is the newly estimated residual actuator vector. The idea behind the loop gain is that applying the full correction to the DM may drive the servo loop to be unstable in closed loop operation, especially at low SNR. In the simulations, the loop gain value is typically close to 1 for good SNR and reduced to 0.1 for faint targets. The low loop gain value is equivalent to averaging over longer times. An example of wavefront correction is shown in Fig. 16.

Although the piston term is not taken into account in the simulation, in reality it is important for interferometry. The AO system is insensitive to piston and will not be able to correct it. In fact in interferometry, AO systems should avoid inducing relative extra piston between telescopes. One way to reduce the induced piston is to monitor the DM corrections on each telescope and make sure the actuators stay around the mid range of their travel distance. As long as the induced relative piston is not significant compared to the atmospheric piston, the OPLE system will still be able to track the fringes.

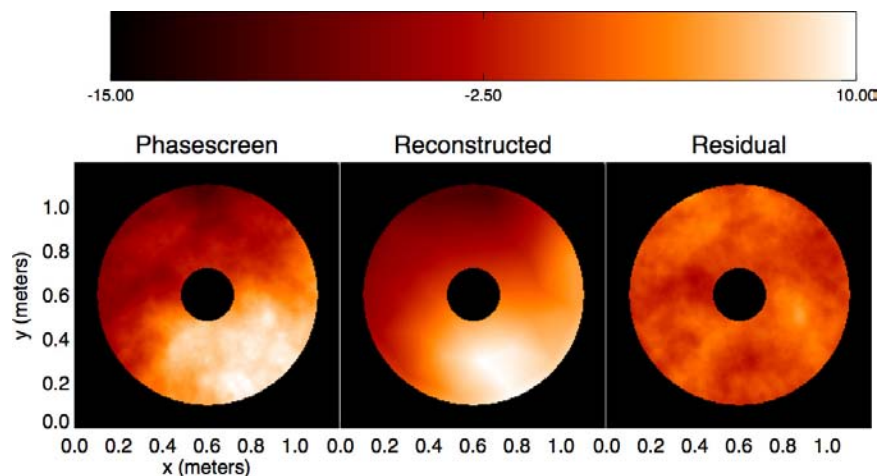


Fig. 16. An example of wavefront reconstruction. The units for the color lookup table is in radian at 0.55 micron.

Table 2. The three configurations used in the simulations.

	Lenslet configuration	DM configuration
Configuration 1	18-lenslet	31-actuator
Configuration 2	36-lenslet	31-actuator
Configuration 3	36-lenslet	61-actuator

5.6. Performance simulation

In order to find the best DM and lenslet configuration for the CHARA array, we run the simulations for a few different configurations. For instance, more subapertures will give better correction for bright targets in bad seeing, but this will compromise the faint target tracking limits. Also, a 61-actuator DM version will perform better than a 31-actuator DM, but also costs more. The three configurations considered for detailed study are summarized in Table 2. In addition, two different seeing conditions at wavelength 0.5 micron are considered: effective $r_0 = 12 \text{ cm}/t_0 = 10 \text{ ms}$, and effective $r_0 = 6 \text{ cm}/t_0 = 2.3 \text{ ms}$. These two cases represent 80th and 20th percentile of summer seeing at Mt. Wilson.

The results are reported in two parameters: the traditional Strehl Ratio, and coupling into a single-mode fiber. Both of them are measured in H band.

5.7. Main results

Figure 17 shows the main results of the performance studies. The AO system improves the light throughput significantly for bright targets, but barely for faint ones at $R = 16$ magnitude. Phase I AO (TT only) can improve the light throughput by a factor of up to 2.5–3 when coupling to a single-mode fiber in H band, and drop to half of that at $R \sim 15$. Full AO correction can improve by a factor of 4–7, and drops to half at $R \sim 12$ for bad seeing and 14 for good seeing. The performance of 36-subaperture configuration is better than 18-subaperture configuration above $R_{\text{mag}} = 12 \text{ mag}$ especially during bad seeing, but slightly worse for very faint objects during good seeing. The improvement in Strehl ratio is marginal when using 61-actuator DM compared to the 31-actuator.

6. Summary

The CHARA array has been funded to install Phase I AO system to each of six telescopes, which performs a full tip/tilt correction. The design of Phase I AO includes two parts: Optical Feed System and Wavefront Sensor, both of which will be installed on telescopes. The Optical Feed system will reflect and guide part of the incoming

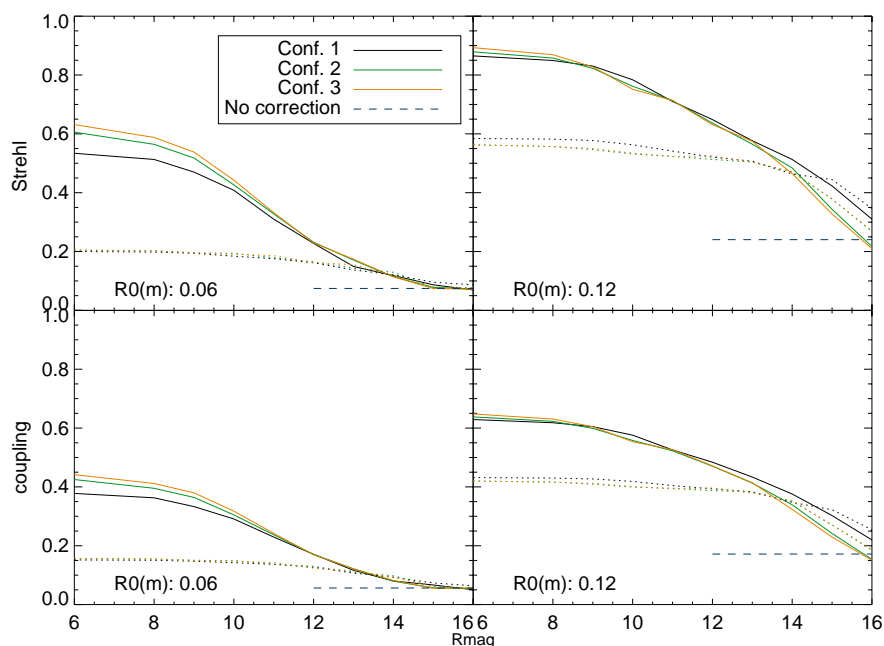


Fig. 17. Final results of the simulations for a range of seeing conditions (measured at $\lambda = 0.5$ micron) and all three configurations. The solid lines represent full AO correction, and dotted lines tip/tilt correction. The Strehl and coupling ratio are both measured in H band.

beam to the acquisition camera and Wavefront Sensor, and let the rest of the beam propagate to the beam combination laboratory. The Wavefront Sensor will measure the atmospheric aberration and send tip/tilt signals to the secondary for a full tip/tilt correction. In Phase II AO, a fast deformable mirror will be implemented to close the loop for full AO correction. The simulation shows that during bad seeing, tip/tilt only correction can improve the light throughput in H band up to a factor of 3, and full AO correction a factor of up to 7. And during good seeing, the same values are 2.5 and 4. The 36-lenslet configuration is more optimal for bright targets ($R < 12$ mag) during bad seeing, and the 18-lenslet configuration is better for faint targets during good seeing.

Acknowledgments

We acknowledge the important feedbacks from the review panel: Chris Shelton, Brent Ellerbroek, and Christoph Baranec, and the discussion with Dave Mozurkewuch and Peter Tuthill. The CHARA Phase I AO is funded by the National Science Foundation under Grant AST-1106136. The CHARA array, operated by Georgia State

University, was built with funding from National Science Foundation, Georgia State University, the W. M. Keck Foundation, and the David and Lucile Packard Foundation. It is currently partially funded by the National Science Foundation under Grant AST-0606958.

References

- Che, X., Monnier, J. D., Kraus, S. *et al.*, 2012, *Proc. SPIE*, **8445**, 84450Z.
- Ireland, M. J., Mrand, A., ten Brummelaar, T. A. *et al.*, 2008, *Proc. SPIE*, **7013**, 701324.
- Lhom, E., Scott, N., ten Brummelaar, T. *et al.*, 2012, *Proc. SPIE*, **8445**, 84452I.
- Mourard, D., Challouf, M., Ligi, R. *et al.*, 2012, *Proc. SPIE*, **8445**, 84450K.
- Monnier, J. D., Baron, F., Anderson, M. *et al.*, 2012, *Proc. SPIE*, **8445**, 84451I.
- Ridgway, S. T., McAlister, H. A., ten Brummelaar, T. A. *et al.*, 2008, *Proc. SPIE*, **7013**, 70133B.
- Sturmann, J., ten Brummelaar, T. A., Ridgway, S. T. *et al.*, 2001, *AAS*, **33**, 876.
- ten Brummelaar, T. A., McAlister, H. A., Ridgway, S. T. *et al.*, 2005, *ApJ*, **628**, 453.
- ten Brummelaar, T. A., McAlister, H. A., Ridgway, S. T. *et al.*, 2008, *Proc. SPIE*, **7013**, 701307.
- ten Brummelaar, T. A., Sturmann, L., Sturmann, J. *et al.*, 2012, *Proc. SPIE*, **8447**, 84473I.